Ebmeier, S. K., Elliott, J. R., Nocquet, J. M., Biggs, J., Mothes, P., Jarrín, P., Yépez, M., Aguaiza, S., Lundgren, P., & Samsonov, S. V. (2016). Shallow earthquake inhibits unrest near Chiles–Cerro Negro volcanoes, Ecuador–Colombian border. *Earth and Planetary Science Letters*, *450*, 283-291. https://doi.org/10.1016/j.epsl.2016.06.046

Shallow earthquake inhibits unrest near Chiles-Cerro Negro volcanoes, Ecuador-Colombian border

Susanna K. Ebmeier[1,2*], John R. Elliott[3,2], Jean-Mathieu Nocquet[4], Juliet Biggs[1], Patricia Mothes[5], Paúl Jarrín[5], Marco Yépez[5], Santiago Aguaiza[5], Paul Lundgren[6] & Sergey V. Samsonov[7]

*s.k.ebmeier@leeds.ac.uk
j.elliott@leeds.ac.uk
nocquet@geoazur.unice.fr
Juliet.biggs@bristol.ac.uk
pmothes@igepn.edu.ec
pjarrin@igepn.edu.ec
myepez@igepn.edu.ec
saguaiza@igepn.edu.ec
Paul.R.Lundgren@jpl.nasa.gov
sergey.samsonov@canada.ca

[1] COMET, School of Earth Sciences, University of Bristol, Queen's Road, Bristol, BS8 4JG, UK
[2] Now at School of Earth and Environment, University of Leeds, LS2 9JT, UK.
[3] COMET, Department of Earth Sciences, University of Oxford, South Park Road, OX1 3AN, UK
[4] Geoazur, IRD, Université de Nice Sophia-Antipolis, Observatoire de la Côte d'Azur, CNRS, 250, Rue A. Einstein, 06560 Valbonne, France.
[5] Instituto Geofisico – Escuela Politécnica Nacional, Ladrón de Guevara, E11-253, Aptdo. 2759 Quito, Ecuador.
[6] Jet Propulsion Laboratory, M/S 300-233, 4800 Oak Grove Drive, Pasadena, CA 91109, USA.
[7] Canada Centre for Mapping and Earth Observation, Natural Resources Canada, 560 Rochester Street, Ottawa, ON K1A 0E4 Canada.

Abstract

Magma movement or reservoir pressurisation can drive swarms of low-magnitude volcano-tectonic earthquakes, as well as occasional larger earthquakes (> M 5) on local tectonic faults. Earthquakes > M 5 near volcanoes are challenging to interpret in terms of evolving volcanic hazard, but are often associated with eruptions, and in some cases enhance the ascent of magma. We present geodetic observations from the first episode of unrest known to have occurred near Chiles and Cerro Negro de Mayasquer volcanoes on the Ecuador-Colombian border. A swarm of volcano-tectonic seismicity in October 2014 culminated in a M_w 5.6 earthquake south of the volcanoes. Satellite radar data spanning this earthquake detects displacements that are consistent with dextral oblique slip on a reverse fault at depths of 1.4—3.4 km within a SSW-NNE trending fault zone that last ruptured in 1886. GPS station measurements capture ~ 20 days of uplift before the earthquake, probably originating from a pressure source ~10-15km south of Volcán Chiles, at depths exceeding 13 km. After the M_w 5.6 earthquake, uplift ceased and the rate of seismicity began to decrease. Potential mechanisms for this decline in activity include a decrease in the rate of movement of magma into the shallow crust, possibly caused by the restriction of fluid pathways. Our observations demonstrate that an earthquake triggered during volcanic unrest can inhibit magmatic processes, and have implications for the hazard interpretation of the interactions between earthquakes and volcanoes.

Highlights (3—5, 85 characters)

- 2014 unrest at Chiles-Cerro Negro culminated in M_w 5.6 earthquake
- Slip was shallow and consistent with El Angel fault zone
- Earthquake was preceded, and potentially triggered, by mid-crustal pressurisation
- The M_w 5.6 earthquake coincided with cessation of uplift and start of fall in seismicity
- Earthquakes during volcanic unrest may inhibit the driving magmatic process

Introduction

1. Earthquakes during volcanic unrest

Volcano Tectonic (VT) seismicity is common during volcanic unrest and eruption (e.g. Roman & Power, 2011) and usually consists of low-magnitude (<M4) earthquakes (e.g., Benoit & McNutt, 1996). Swarms of VT earthquakes have preceded many major explosive eruptions, with the highest rate of seismicity occurring at the onset of eruption (White & McCausland, 2016). More rarely, magmatic processes can trigger larger earthquakes on local tectonic faults. Earthquakes greater than magnitude 5 at volcanoes (listed in Supplementary Table 1) are associated with significant perturbations to subsurface stress fields (e.g., Mt St Helens, 1980; Benoit & McNutt, 1996). This may involve static stress changes from the propagation of a dyke in the shallow crust (e.g., 2000 Miyakejima intrusion; Toda et al., 2002 or 1976 Krafla dyking episode; Pasarelli et al., 2013) and most such examples take

67 place during episodes of rifting with high rates of deformation (e.g., Wright et al., 2006; Biggs et al.,
68 2009; 2013). Earthquakes > M5 have also been recorded during unrest at active volcanoes, where
69 movement of magma or hydrothermal fluids is inferred from deformation, gas emission or seismicity
70 (e.g., at Akutan & Peulik, Lu & Dzurisin, 2014; at Yellowstone, Wicks et al., 2006; near Sabancaya,
71 Jay et al., 2014).

72 The largest group of earthquakes > M 5 at volcanoes occur before, during or shortly after
73 eruptions, and include some events with non-double couple focal mechanisms (Shuler et al., 2013).
74 Earthquakes > M 5 normally occur during explosive phases of eruption (e.g. at Chaiten in 2008, Wicks
75 et al., 2011), although some have been attributed to post-eruptive stress readjustment (e.g., 1962 and
76 1983 at Miyakejima, Yokoyama, 2001) and caldera floor collapse (Riel et al., 2015).

77 VT swarms that include earthquakes > M 5 may also precede eruption, as occurred before the 1999
78 eruption of Shishaldin (Moran et al., 2002). In some cases, such earthquakes may also play a more
79 active role in triggering eruption. For example, a sequence of three M_w 5.2 events before the 1999
80 eruption of Cerro Negro, Nicaragua is thought to have reduced minimum principal stress and thus
81 facilitated the ascent of magma (Diez et al., 2005).

82 The interpretation of earthquakes during volcanic unrest in terms of developing hazard is
83 challenging. As the majority of reported > M 5 earthquakes have been associated with major
84 eruptions, the initial interpretation of such events would reasonably be one of increasing hazard. Here
85 we use geodetic measurements during unrest near two volcanoes on the Ecuador-Colombian border,

86 Chiles and Cerro Negro, to observe deformation before and after a M_w 5.6 earthquake and examine the
87 relationship between magmatic intrusion and fault rupture.
88
89 **2. Volcán Chiles & Cerro Negro de Mayasquer**
90 Volcán Chiles and Cerro Negro de Mayasquer are stratovolcanoes that straddle the Ecuador-
91 Colombian border and have had no recorded historical eruptions (Figure 1A-B). Volcán Chiles last
92 erupted about 160,000 years ago whilst andesitic and dacitic lava flows in Cerro Negro caldera are
93 possibly of Holocene age. The most recent erupted material to have been dated from either volcano
94 comes from a debris avalanche at Cerro Negro and is at least 3000 years old (Cortés & Calvache,
95 1997). An active geothermal system extends to the south of Chiles, manifesting in numerous hot
96 springs (Figure 1C, Instituto Geofisico, 2014, No. 27). Their lack of historical activity and remote
97 location on an international border have meant that until 2013, both volcanoes were monitored with
98 minimal instrumentation, and were classified as 'potentially active' by the Instituto Geofisico ('IG',
99 Escuela Poltecnica Nacional,) and 'active but stable' by the Pasto Volcano Observatory, Servicio
100 Geologico Colombiano ('SGC'). Low-level seismicity (<10 VT and low frequency events per month)
101 was reported at Chiles-Cerro Negro from 1991 onwards, when the IG installed a single seismometer,
102 and has been attributed to an active hydrothermal system (Ruiz et al., 2013).
103 In October 2013, a seismic swarm consisting of >1000 recorded events per day occurred 2-6 km
104 south of Chiles. Two further VT swarms took place in February-May 2014 and September–December
105 2014. The SGC changed the volcanoes' alert level from green ('active but stable') to yellow ('changes

106 to the volcano's activity') in April 2014, in response to the increase in the rate and magnitude of VT
107 earthquakes (SGC, Boletín Mensual No. 04-2014). The 2014 VT swarms had increasing duration and
108 event rate, but were separated by periods of low-level seismicity of the order of 10s to 100s of events
109 per day. The majority of the earthquakes had depths of between 2 and 5 km, were < M 4, and
110 concentrated in a ~25 km^2 area to the southwest of Chiles (Figure 1C). All three swarms occurred in
111 approximately the same location, and larger events (M 3-4) occurred later, rather than at the beginning,
112 of each sequence. These 'swarm-like' characteristics are more likely to be associated with pore-fluid
113 pressure changes than by cascading elastic failures (Vidale et al., 2006) and are similar in this respect
114 to VT seismicity at many other volcanoes (White & McCausland, 2016). The Chiles-Cerro Negro
115 seismic swarms were dominated by high frequency events thought to be associated with brittle failure,
116 but there were also low frequency components to some waveforms later in the unrest that could
117 indicate fluid movement (Ruiz et al., 2013; Salvage, 2015).
118 In October 2014, there were > 5000 small earthquakes detected per day (Figure 2), including some
119 long period events (e.g., Chouet and Matoza, 2013). At this time, some of the larger earthquakes were
120 felt in Tulcán and Tufiño in Ecuador (IG, Informe del Volcán Chiles – Cerro Negro No. 23), and by
121 residents of the Resguardos Indígenas del Municipio de Cumbal in Colombia (SGC, Boletín Mensual
122 No. 10-2014). On the 20th October at 19:33 UTC a M_w 5.6 earthquake caused damage to buildings in
123 villages near Volcán Chiles (IG, Informe del Volcán Chiles – Cerro Negro No. 23). The escalation in
124 the rate and increase in maximum magnitude of the seismic swarms, as well as the M_w 5.6 earthquake
125 were interpreted as evidence for the ascent of magma. Both the IG and the SGC changed their

assessment of the volcano activity level from yellow to orange, meaning that an eruption was expected within days to weeks. The number of VT earthquakes per day reached their maximum on the 24th October, four days after the M_w 5.6 earthquake, and presumably encompassing aftershocks from the larger event. After this, the number of earthquakes per day started to decline and had gradually returned to background levels by May 2015 (Figure 2), suggesting a cessation of magma ascent (e.g., Moran et al., 2011). There were no changes considered significant relative to background levels in the pH or temperature of hot springs monitored by the IG (locations marked on Figure 1C), or in fumerolic activity on the western side of Cerro Negro's crater (Instituto Geofisico, 2014, No. 27). In response to the decrease in seismicity, GPS deformation and InSAR measurements of the M_w 5.6 earthquake, the volcanic alert level was returned from orange ('eruption anticipated within days to weeks') to yellow (SGC: 'changes to the volcano's activity' and IG: 'potentially active') by both the SGC and IG on 26th November 2014.

3. Data & Methods

3.1 GPS data 1st -19th October 2014

We analysed GPS data from the IG tectonic network station COEC, located ~15 km to the southeast of the volcanoes and from a second site, CHLS, installed ~2 km from Volcán Chiles on 10 May 2014 (Figure 1). We use GAMIT 10.6 (King & Bock, 1999) to process the GPS data from CHLS and COEC with an Ecuador wide continuous GPS network (Mothes et al., 2013). Each daily solution is first transformed into the International Terrestrial Reference Frame ITRF2008 (Altamimi et

146 al., 2011) using a 7-parameter transformation. Final time series (Figure 3) are expressed in a north
147 Andean Sliver reference frame by removing the trend predicted by the Euler pole proposed by Nocquet
148 et al., (2014).

149 CHLS and COEC stations recorded displacements between the 1st and 19th October 2014
150 indicative of pressurisation to the south of the volcanoes. TerraSAR-X interferograms that spanned this
151 time period do not extend far enough south to capture this signal (Supplementary Figure 2). We
152 therefore used the 3D displacements from both GPS stations to find the horizontal location and depth
153 of the pressurisation responsible for these displacements. Data from both GPS stations are noisy
154 (especially COEC) and are not in themselves sufficient to constrain a unique source geometry. We
155 therefore used a simple point source, elastic half space model to investigate the potential range of
156 depths for a pressurising source. We consider this a more appropriate interpretation of the data than a
157 model with realistic rheology, topography and source geometry but that requires more degrees of
158 freedom. As the variance in horizontal GPS displacements is much lower than for the vertical
159 displacements, we first used these to find the best-fit latitude and longitude of a point pressurisation
160 source and to identify the horizontal region within which it is likely to be located. We then used a grid
161 search approach, minimising misfit between the predicted and observed GPS displacements, to find the
162 regions of the depth-volume change parameter space within which the early October source could be
163 located (Supplementary Figure 1). We consider solutions with a root mean square error less than 1.5
164 mm (150% of the minimum value, and within the range of standard deviations in GPS daily solutions
165 of 1—3 mm) to be a reasonable fit to the GPS data.

3.2 InSAR analysis of 20th October M_w 5.6 earthquake

We used Interferometric Synthetic Aperture Radar (InSAR) to measure displacements during the October 2014 swarm. Deformation was captured by four independent interferograms (Supplementary Figure 2) from three satellite instruments: TerraSAR-X (18.10.2014-27.11.2014 descending), CosmoSkymed (28.03.2014-30.10.2014 descending and 14.03.2014-30.10.2014 ascending) and RADARSAT-2 (17.05.2014-01.11.2014 descending). We are confident that the displacements captured in these interferograms primarily represent displacements associated with the M_w 5.6 EQ because two earlier TerraSAR-X images (spanning 03.03.2014—28.05.2014 and 28.05.2014—18.10.2014) show no deformation above a magnitude of ~ 1 cm, despite continued low-magnitude seismicity. Interferograms were constructed using ISCE (Rosen et al., 2011) and GAMMA software (Wegmuller et al., 1998), and topographic contributions to interferogram phase were corrected using the 30 m SRTM DEM (Rosen et al., 2001). Unwrapping was carried out using the Snaphu algorithm (Chen & Zebker, 2002).

All four interferograms were downsampled using nested uniform sampling (1800 m pixels) with a higher sampling density (400 m pixels) over the regions of high magnitude deformation (Supplementary Figure 3). We model the line-of-sight displacements as dislocations from uniform slip on a rectangular fault plane in an elastic half-space (Okada et al., 1985) and take $\lambda = \mu = 3 \times 10^{10}$ Pa as the Lamé parameters. We jointly invert the downsampled line-of-sight displacements from all four interferograms for uniform slip on a single fault. First, to constrain the fault geometry, we invert all four interferograms and solve for slip, strike, dip, rake, surface centre location, length, and top and

bottom depths. We estimate errors on these parameters by performing a Monte Carlo analysis where the inversion was performed 250 times on data sets perturbed by randomly generated synthetic noise with the same variance and e-folding distances (Hanssen, 2001) as the data (Supplementary Table 2, Supplementary Figure 4). We next refine our model by solving for distributed slip on the best-fit fault plane. The data are inverted using a non-negative least squares algorithm and Laplacian smoothing (e.g., Funning et al., 2005). We extend the length and height of the fault plane and divide into patches of side length 0.5 km, solving linearly for variable slip and rake on each patch, which has a fixed geometry (Funning et al., 2005).

3.3 Stress change modelling

Faults can be brought closer to failure by an increase in Coulomb stress, $\Delta\sigma_C = \Delta\tau - \mu'\Delta\sigma_N$, either through (1) an decrease in normal stress, $\Delta\sigma_N$, ('unclamping'), (2) an increase in shear stress, $\Delta\tau$, and/or (3) a decrease in the effective coefficient of friction (μ') on the fault plane (Stein, 1999; Jolly & McNutt, 1999).

We investigate the stress and strain changes generated by both point pressurisation sources that match the early October GPS displacements and the M_w 5.6 earthquake using the United States Geological Survey code Coulomb 3.1 (Lin & Stein, 2004). As the location of the early October pressurisation is poorly constrained by the GPS data, we investigate the stress changes caused by a range of different point source locations at intervals of ~0.02° within the ranges of 0.64°N-0.74°N latitude and 78.0°W-77.9°W longitude. For each horizontal location we also test a range of depths (10,

15, 20, 25 km) and corresponding volume changes (Supplementary Figure 1), assuming $\mu' = 0.4$. We estimate Coulomb stress changes for each case on our preferred fault plane for the M_w 5.6 earthquake.

We investigate whether uncertainties in the estimated fault strike of +/- 2°, (1σ errors, Supplementary Figure 4), and corresponding variations in fault position and geometry, have an impact on the Coulomb stress changes for a given point pressurisation location, depth and volume, but find that differences are negligible. The differences in strains predicted by the uniform and distributed slip solutions are also negligible.

4. Results

Between the 1st and 19th October 2014, CHLS was displaced northward (9 +/- 2 mm) and upwards (15 +/- 9 mm), coincident in time with eastward displacement (6 +/- 3 mm) at COEC (Figure 3), all relative to the North Andean Sliver (Nocquet et al., 2014). Other components of displacement over this time were lower than average uncertainties in daily solutions of ~2-3 mm horizontal displacement and ~8-9 mm vertical displacement (95% confidence level). No deformation was reported from either GPS site before the 1st October 2014 (although CHLS was installed only on 10th May 2014). The TerraSAR-X interferograms that extended from 28th May to 18th October (144 days) also show no deformation at either volcano or in the location of the VT swarm (but did not extend as far south as our preferred early October inflation source location, Figure 1). The displacements recorded at the GPS stations were of similar magnitude (CHLS 1st-19th October is equivalent to ~13 mm in TSX line of sight) to the variance in interferogram phase (~10 mm) and are not apparent in the

226 coherent patches of the interferograms. After the M_w 5.6 earthquake on 20th Oct, displacements
227 appeared to cease at both GPS stations. Average displacement rates over the twenty days afterwards
228 were lower than average uncertainties in daily solutions, except for the northward displacement of
229 CHLS, which may have continued for a few days at a much lower rate than before the earthquake.
230 The trends of northward and vertical displacement at CHLS between the ~1st and 19th October
231 are well above the uncertainties in daily solutions, and show that the source certainly lies to the south
232 of the GPS station (Figure 1B), rather than at Volcán Chiles itself or at the densest part of the seismic
233 swarm (Figure 1C). The direction of movement of COEC is also clearly eastward until the M_w 5.6
234 earthquake on 20th October, when it reversed to westward. This change in direction at COEC but not
235 CHLS means that GPS displacements are unlikely to be related purely to slip on the fault that ruptured
236 during the M_w 5.6 earthquake. Deformation can also not be attributed to the cumulative slip of the
237 thousands of < M 4 VT earthquakes during 1-19th October: the earthquakes are distributed over a broad
238 area of ~10 km^2 west of the GPS stations and have a cumulative magnitude of only ~M 4.
239 Our analysis shows that GPS displacements are matched by pressurisation at ~(-77.95°W,
240 0.67°N) at depths exceeding 13 km and less than 25 km (Figure 1B, Supplementary Figure 1). The
241 horizontal location of such a pressure source could vary over ~5 km while still fitting the GPS data to
242 within 3 mm. We do not have good constraints on volume change because we do not know reservoir
243 and magma compressibility or the temperature profile of the crust (and therefore viscoelasticity).
244 Alternative source geometries such as an ellipsoid (Yang et al., 1988, 8 free parameters) or sill (Okada,
245 1985, 8 free parameters) would also need to be located in the mid-crust (> 10 km) to satisfy the low

246 magnitude of upward GPS displacements (15 +/-5 mm and 6 +/-4 mm at CHLS and COEC,
247 respectively). The GPS displacements could potentially also be produced by the opening of a dyke,
248 though this would have to have been deep enough that opening could be accommodated without
249 seismicity. The only cluster of earthquake locations during 1st—19th October was to the east of CHLS
250 (Figure 1C), mostly between 2 and 6 km depth. A dyke intrusion in the shallow crust in this region
251 could not have produced the observed GPS displacements, and would also have caused a measureable
252 deformation signal in the interferograms, which were coherent in this area and showed no
253 displacements up to 18th October 2014.
254 The InSAR displacements spanning the 20th October EQ are well matched by 1.2 m of slip on
255 a fault of strike = 213+/-2°, dip = 50+/-1.6°, rake = 151+/-2.4°, length = 3.4 km, giving a moment
256 equivalent to an earthquake of M_w 5.6 (Figure 4). The modelled rupture was shallow, between depths
257 of 3.4 and 1.4 km, and the southern edge of the fault rupture lies > 6 km north and at least 10 km
258 shallower than the early October source. Comparison of the root mean squared misfit for inversion
259 with slip fixed at intervals show that misfit decreases with increasing slip up to a value of 0.8 m, after
260 which misfits level off. However, the model fit to the maximum co-seismic displacements, over the
261 footwall of the fault, is best for slip of 1.2 m. Our preferred fault plane solution implies a relatively
262 high stress drop of 14 MPa, but this could vary by +/- 3 MPa (Supplementary Figure 4), and could
263 therefore be as low as 10 MPa. The auxiliary plane solution (dipping to southeast) does not provide as
264 good a match to the data as our preferred solution (e.g. RMS of residuals was 0.2 cm higher for
265 CosmoSkyMed and TerraSAR-X interferograms).

Our variable slip and rake solution for fixed geometry (Figure 5A) demonstrates that the slip at the south-western end of the fault was almost pure right-lateral, and that the reverse component of slip became more significant in the northeast. Our InSAR derived focal mechanism is in reasonable agreement with the IPGP seismological analysis (Vallée et al., 2011) of the waveform (M_w 5.7 and strike 224°, dip 62° and rake 163°), although fault locations differ by ~30 km, which is within the range of error (10—30 km) expected for global seismological locations (e.g., Elliott et al., 2010).

Whether or not the modelled early October pressurisation would have brought this fault closer to failure depends on its location: some acceptable source locations increase Coulomb stress ($\Delta\sigma_C$) on the fault plane, while others lower it. Normal stress change across almost the whole fault plane is negative (1—10 kPa, unclamping) for pressurisation at locations within the bounds of models constrained by GPS measurement, but shear stresses on different parts of the fault vary in magnitude and sign (~-5-5 kPa). At the part of the fault plane closest to the magmatic intrusion, slip is close to pure right-lateral, so we estimate Coulomb stress change for right-lateral motion and find that $\Delta\sigma_C$ is positive for early October pressurisation sources located at the northern side of the range required by GPS measurements (10-30 kPa on southwestern corner of the fault, e.g., Figure 5B-C). A more complex source geometry (e.g. an opening sill or pressurising prolate ellipsoid) could potentially generate quite different stress fields (see Albino & Sigmundsson, 2014), but these would also be sensitive to position and trade-offs between depth and volume change or opening. It is therefore possible, but not certain, that the static stress changes contributed to triggering the M_w 5.6 earthquake. The earthquake itself caused an increase in dilational strain west and east of the fault plane, but resulted

286 in a lobe of negative dilational strain (volumetric compression) in the upper crust in the vicinity of the
287 early October pressurisation (Figure 6B).

288 For pressurisation near our best-fit location, we estimate that $\Delta\sigma_N$ and $\Delta\tau$ on the fault are of the
289 same order of magnitude, making $\Delta\sigma_C$ very sensitive to small changes in the effective coefficient of
290 friction, μ', and therefore pore pressure. Pressurisation of the early October source also caused dilation
291 in the surrounding crust (Figure 6A) and may have caused an increase to the flow of fluids into the
292 hydrothermal system. Elevated pore fluid pressure may both have reduced the effective friction on the
293 El Angel zone fault, and contributed to the increase in the rate of VT seismicity before the 20th
294 October. Our estimations of Coulomb stress changes are within the range thought to cause variations
295 in rates of seismicity due to hydrological loading (2-4 kPa; Bettinelli et al., 2008) and in rates of
296 volcanic tremor due to fluid tides (15 kPa; Rubinstein et al., 2008).

297

298 ## 5. Discussion

299 ### 5.1 Mid-crustal magmatic source

300 GPS displacements from 1st -19th October 2014 are best matched by a pressurising source
301 within a ~5 km radius of (-77.95°, 0.67°) at depths of >13 km. The source location is constrained by
302 only two GPS stations, so the uncertainty in its location is high, but we are confident that 1) it lies to
303 the south of CHLS and west of COEC and 2) that it is at least at mid-crustal depths. Because the GPS
304 data indicate a pressurisation at mid-crustal depths, we interpret it as evidence for magma reservoir

pressurisation, rather than a hydrothermal process. The volume, or even lateral extent, of the magma reservoir associated with the Chiles-Cerro Negro unrest is, however, unclear.

There has been no prior indication of an eruption at the above modelled early October pressure source location. The surface of this area is covered with old (>10,000 years), poorly studied volcanic deposits and to our knowledge has not been the site of historical seismic swarms. After Chiles-Cerro Negro (~15km north of the early October pressure source), the next nearest Holocene volcanoes are > 40 km away (Chachimbiro, ~45 km WSW; Imbabura ~50 km SW and Soche, ~45 km, ESE). However, deformation located tens of kilometres away from the nearest known volcanic centre is a common observation in regional InSAR surveys (e.g., Pritchard & Simons, 2004; Biggs et al., 2011; Lundgren et al., 2015) and distal VT seismicity up to 15 km away from the associated volcano is also a common observation at the onset of both eruptions and intrusions (White & McCausland, 2015).

5.2 Origin of the M_w 5.6 earthquake

The M_w 5.6 earthquake occurred on a fault aligned with a SSW-NNE trending system in an extension of the Romeral fault in Colombia (e.g., Ego et al., 1996). Two large earthquakes occurred on this fault system in August 1868 near the towns of El Angel (at ~-77.9°W, 0.7°N) and Ibarra (at ~-78.45°W, 0.36°N), with magnitudes in the range 6.4-6.8 and 7.1-7.7 respectively, as estimated from intensity data (Beauval et al., 2010). The regional strain field is dominated by the subduction of the Nazca plate at a rate of ~46 mm/yr (Nocquet et al., 2014) and deformation within the North Andean Sliver. The direction of maximum compressive stress derived from focal mechanism inversion for

historical earthquakes <60 km depth in the Romeral fault area is ~076°N (Ego et al., 1996), which is in reasonable agreement with a horizontal direction of displacement of 052°N from the 2014 M_w 5.6 earthquake. The M_w 5.6 earthquake was on an active fault that had potentially been locked at least since 1868, and is likely to have been stressed before the unrest in 2014.

It is unlikely that the M_w 5.6 earthquake occurred during the 2014 Chiles-Cerro Negro swarm by coincidence. Between 1980 and the end of 2015 there were only 9 earthquakes > M 5 at depths < 50 km within a 100 kilometres radius of Chiles-Cerro Negro volcanoes (Supplementary Table 2). The M_w 5.6 earthquake was preceded by an acceleration in the rate of seismicity (Salvage, 2015), suggesting that the same underlying process drove both the VT swarm and triggered the M_w 5.6 earthquake.

5.3 Elevated pore-fluid pressure in the shallow crust

Our Coulomb stress calculations show that static stress changes from magma movement in October 2014 could potentially have brought the El Angel fault closer to failure, but the impact of mid-crustal magmatic activity on the hydrothermal system that feeds the multiple hot springs south of Chiles and Cerro Negro may have been equally or more important. The swarm-like characteristics of seismicity at Chiles-Cerro Negro are indicative of elevated pore-fluid pressure (e.g., Vidale et al., 2006), which could be either due to heating of groundwater, or the ascent of magmatic fluids (Jolly & McNutt, 1999). The deep magmatic intrusion in early October caused dilation (Figure 6), which may have increased the flow of magmatic fluids into the hydrothermal system, elevating pore fluid pressure.

345 Both the majority of the VT events during the 2013-2014 unrest, and the fault that ruptured in the M_w
346 5.6 earthquake lie at depths (2-6 km). This is consistent with a shallow hydrothermal system to which
347 background seismicity at Chiles and Cerro Negro has been attributed (Ruiz et al., 2013; Cortés &
348 Calvache, 1997).
349
350 **5.4 The impact of the M 5.6 earthquake: suppression of unrest**
351 The 20th October M_w 5.6 earthquake coincided with the cessation of the uplift seen in GPS
352 measurements, and preceded the start of a gradual decrease in number of seismic events per day after
353 24th October (Figures 2 and 3). IG catalogue earthquake locations suggest that more earthquakes, with
354 higher average magnitudes, occurred closer to the northern end of the M_w 5.6 fault plane during the
355 four days after the 20th October than the four days before (Supplementary Figure 6). The rate of decay
356 in seismic event count after this time is likely to encompass contributions from an aftershock sequence
357 from the M_w 5.6 earthquake, as well as a more gradual decrease in VT seismicity from pre-20th October
358 levels. Since October 2015, both GPS stations and repeated satellite radar measurements of the region
359 around Chiles and Cerro Negro show no evidence of further deformation.
360 A possible explanation is that the M_w 5.6 earthquake affected the subsurface stress field so that
361 it changed how magmatic processes were accommodated. For example, a transition from an earlier
362 upward migration into the elastic crust, to a deeper, lateral movement of magma would diminish any
363 measurable deformation. Strain changes caused by the earthquake (Figure 6B) may also have brought
364 about a change to the pattern of fluid flow, potentially restricting the migration of fluids into the

365 hydrothermal system; increasing the flow of hydrothermal fluids out and therefore decreasing pore-
366 fluid pressure. Such shifts in deformation patterns have been recorded during periods of elevated
367 seismicity at both Long Valley (1997-1998) and Yellowstone calderas (1985, 1995) and attributed to
368 changes to the flow of hydrothermal and magmatic fluids caused by tectonic processes (e.g., Hill et al.,
369 2006; Wicks et al., 2006).
370
371 **5.5 Negative feedback on magmatic processes**
372 Large earthquakes have been shown to trigger volcanic unrest (e.g., Pritchard et al., 2013;
373 Takada et al., 2013; Battaglia et al., 2012) and eruption (Linde & Sacks, 1998) by causing static and
374 dynamic stress changes (Manga & Brodsky, 2006). Some detailed case studies have demonstrated
375 positive feedback, where moderate earthquakes and faulting enhance the magmatic processes thought
376 to have triggered them. This can occur during the onset of eruption, for example during the 1999
377 eruption of Cerro Negro in Nicaragua (Diez et al., 2005) or during cycles of trapdoor faulting and sill
378 growth at Sierra Negra in the Galapagos (Jónsson, 2009). During the early stages of dyke intrusion
379 near Lake Natron, slip on a normal fault unclamped the source region of a vertically propagating dyke,
380 but increased clamping at shallower depths. In this case, stresses at the dyke tip were sufficient to
381 overcome clamping effects and allow the vertical propagation of the dyke, so that the net impact of the
382 fault slip on magma ascent was positive (Biggs et al., 2013).
383 Examples of equivalent negative feedback, where earthquakes triggered during volcanic
384 unrest inhibit an underlying magmatic process, appear to be rarer (or at least less frequently reported).

385 However, a recent study, Maccaferri et al., (2015), used mechanical modelling to demonstrate that
386 stress transfer from a M 6.5 earthquake triggered at the tip of a propagating dyke at Miyakejima in
387 2000 was the primary cause for its arrest. Interaction with faulting has also been implicated as an
388 important factor in the arrest of a dyke at Harrat Lunayyir in 2009 (Xu et al., 2016), and is expected to
389 be a widespread process.

390 Although many earthquakes > M 5 have been reported during volcanic unrest (Supplementary
391 Table 1), their relationship to the underlying magmatic process is often unclear (e.g. during VT swarms
392 at Akutan and Peulik; Lu & Dzurisin, 2014). Our observations from near Chiles-Cerro Negro are
393 unusual in that they document a turning point in both VT seismicity and GPS displacement that
394 coincide with a triggered tectonic earthquake. A similar event may have taken place at Iwatesan
395 volcano (Japan) in 1998, when a M 6.1 earthquake occurred during a VT swarm, and was attributed to
396 stress changes from pressurisation ~12 km west of the volcano's summit (Nishimura et al., 2001).
397 Although seismicity and deformation after the earthquake are not documented, Nishimura et al. note
398 that "the volcanic activity came to be calm after the occurrence of the M 6.1 earthquake," which
399 implies that, as at Chiles-Cerro Negro, the earthquake may have inhibited the underlying process that
400 had been driving unrest.

401 Earthquakes initiating an escalation in magmatic activity have been more frequently reported
402 than those causing a diminishment. In particular, many examples of larger earthquakes occurring
403 during VT swarms immediately before eruption mean that larger earthquakes are necessarily
404 interpreted as indicating elevated volcanic hazard. Our observations at Chiles-Cerro Negro

405 demonstrate that in some cases this interpretation results in 'false positives' where no escalation to
406 eruption takes place, and furthermore that such earthquakes may act to inhibit magma movement.
407
408 **Conclusions**
409 The first measured unrest near Chiles-Cerro Negro volcanoes took place in 2013-2014 and
410 consisted of three episodes of VT seismicity and a brief period of uplift in October 2014. After a
411 M_w5.6 earthquake on 20th October 2014, uplift ceased and seismicity began to fall. Our interpretation
412 of the sequence of events at Chiles-Cerro Negro based on our GPS and InSAR measurements from
413 October 2014 is as follows:
414 • The pressurisation of a mid-crustal magma reservoir (>13 km depth, ~ 15km south of Volcán Chiles)
415 caused displacements at two GPS stations 1st-19th October 2014. This pressurisation caused dilation,
416 which may have contributed to increased fluid flow in the hydrothermal system and the observed
417 increase in the rate of VT seismicity.
418 • On the 20th October a M_w 5.6 earthquake occurred on a shallow fault in the El Angel fault zone,
419 probably triggered by elevated pore fluid pressure, possibly with some contribution from static stress
420 changes caused by the deep pressurisation.
421 • The earthquake caused strain changes in the subsurface that coincided with (1) the cessation of GPS
422 displacements, (2) a gradual decrease in the rates of VT seismicity. This may have been due to
423 transition in fluid flow and mode of magma storage.
424

425 Our observations at Chiles-Cerro Negro are important because they demonstrate that an earthquake
426 triggered during volcanic unrest can inhibit, rather than enhance, the process driving it. With the
427 exception of dyke propagation during rifting, this effect has not been widely reported. However, it
428 may occur at other volcanoes where active fault zones lie in close enough proximity to volcanic belts to
429 allow interaction with magma reservoirs.
430
431
432
433

Figure 1: A. Location of Chiles and Cerro Negro on the Ecuador-Colombian border. B. Map showing the locations of Chiles & Cerro Negro volcanoes (blue triangles), Quaternary faults (black), best-fit October 2014 point source pressurisation (red star) and uniform slip fault plane solution (red lines). Black arrows at GPS stations, CHLS and COEC, show horizontal displacements for the period of 01.10.2014-19.10.2014. Shaded grey area shows spatial locations that fit a point source to within GPS error. C. Instituto Geofisico catalogue earthquakes locations, depths and magnitudes from stations marked with black squares and stations names for 01.10.2014-19.10.2014 (e.g., Instituto Geofisico EPN, 2014; Ruiz et al., 2013). The locations of hot springs where geochemical monitoring is carried out by IG are indicated by blue squares on a cross hair.

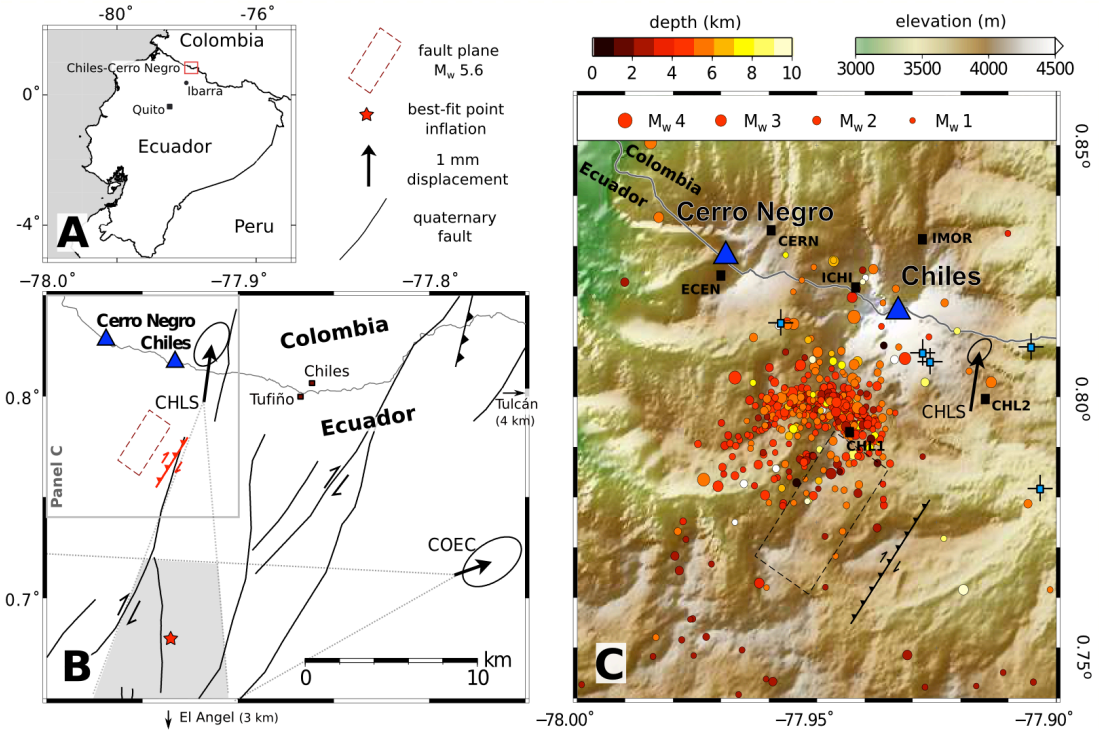

Figure 2: Seismic count from Instituto Geofisico catalogue at Chiles-Cerro Negro between September 2014 and July 2015 (some initial counts, including automatically identified earthquakes that had not yet been quality-controlled, were generally higher and found ~8000 events per day on the 20th October 2014, e.g., Instituto Geofisico EPN, 2014, No. 26). Catalogue earthquakes were located using data from eight seismometers, mostly to the north of the volcanoes, and including those shown on Figure 1C plus ICAN (-77.9505, 0.864333) and IPAN (-77.8805, 0.850667). The grey shaded box shows the period of uplift detected by the GPS and shown in Figure 3.

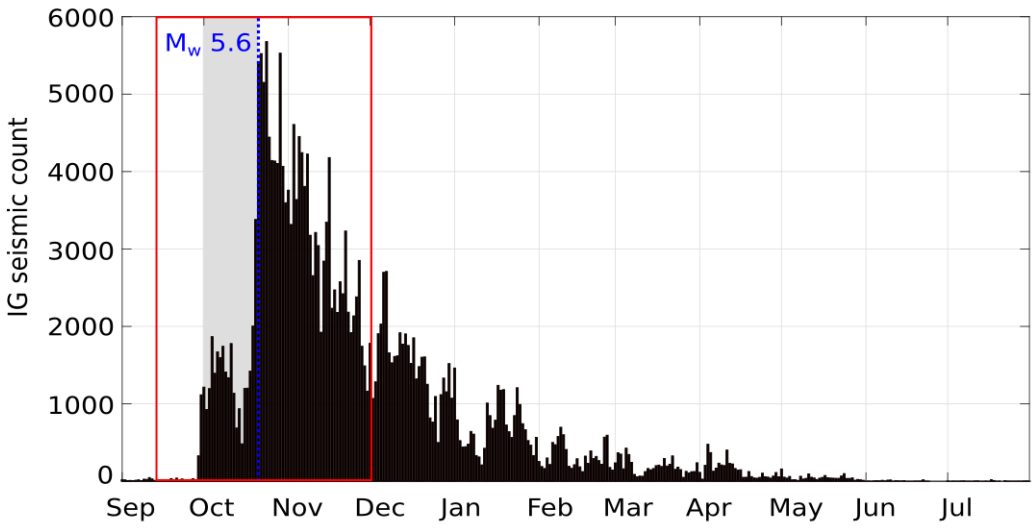

Figure 3: GPS time series displacements (10.09.2014 – 1.12.2014) for stations CHLS (installed 10.05.2014) and COEC. Error bars show 1-sigma errors for the daily solutions. The date of the M_w 5.6 earthquake, 20th October, is indicated by a blue dashed line and the shaded grey box indicates the approximate period of uplift also shown on Figure 2. The seismic count from the Instituto Geofisico catalogue for the same time period is shown in the lower panel.

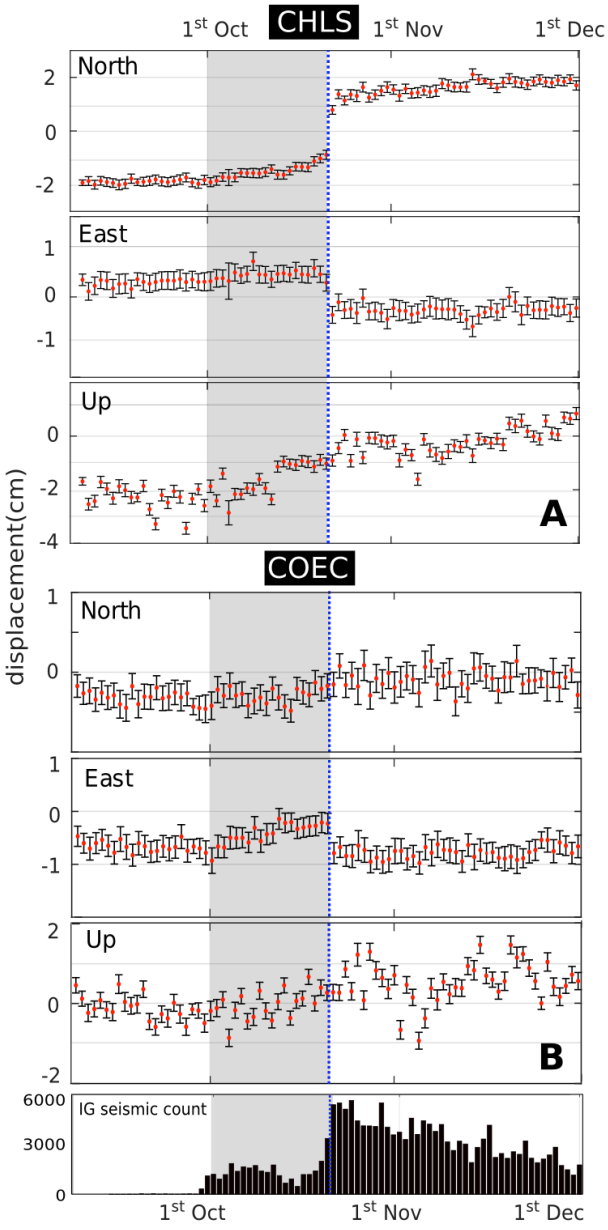

Figure 4: Examples of line of sight InSAR displacements from descending CosmoSkymed (28.03.2014-30.10.2014) and ascending RADARSAT-2 data (17.05.2014 – 1.11.2014). Line of sight (los) azimuth direction and incidence angle are indicated on individual panels. Model panels show the predicted line of sight displacements for our preferred uniform slip solution (strike = 213+/-2°, dip = 50+/-1.6° and rake = 151+/-2.4°, slip = 1.2 m). Line-of-sight displacements (red-blue colour scale) are overlaid onto hill shaded SRTM Topography.

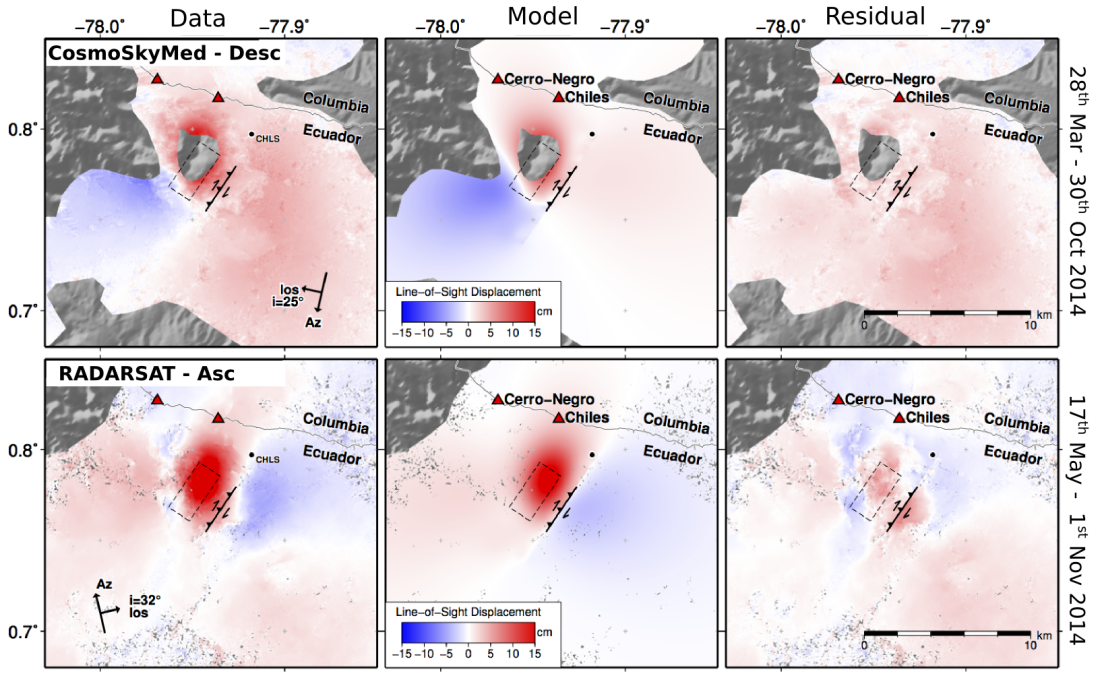

Figure 5: A. Distributed slip solution for slip on a fault plane with the geometry of our uniform slip solution, where slip magnitude and uncertainty is shown by the colour scale and rake by blue arrows. B. Example of Coulomb stress changes for right lateral slip on the plane defined by our uniform slip solution. The dashed box marks the edge of the region of slip and the location of the early October pressurising source is marked with a red outline on part C. C. Source locations for which Coulomb stress change for right-lateral slip on the southwestern corner of the fault plane is positive are indicated by green circles (white circles indicate that Coulomb stress changes are negative).

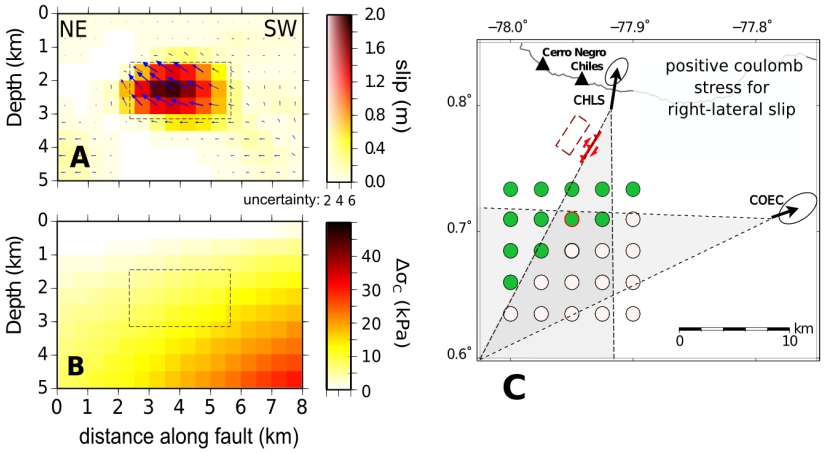

Figure 6: A. Change in dilational strain at 5 km depth for the pressurisation of a point source at our best-fit location and at 13 km depth. B. Change in dilational strain caused by the 20th October M_w 5.6 earthquake at 13 km depth. Blue shows compression and red indicates dilation.

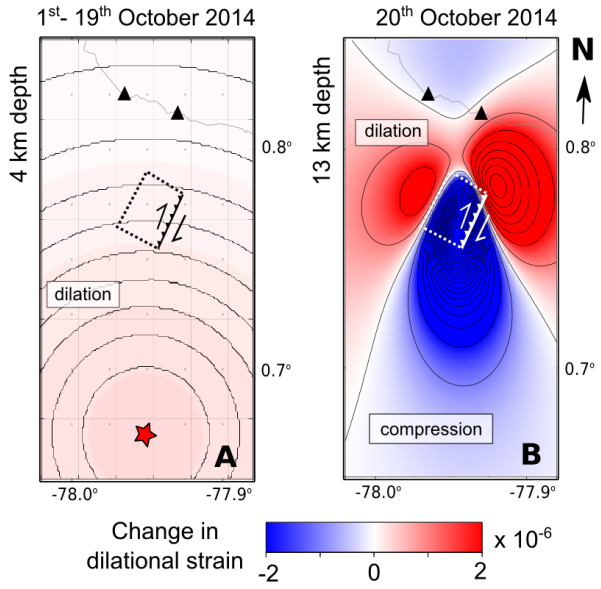

Figure 7: Schematic representation of processes at Chiles-Cerro Negro pre-earthquake (A) 01.10.2014-19.10.2014 and (B) the M_w 5.6 earthquake on 20.10.2014. Blue ellipses indicate the distribution of 90% of VT hypocentres.

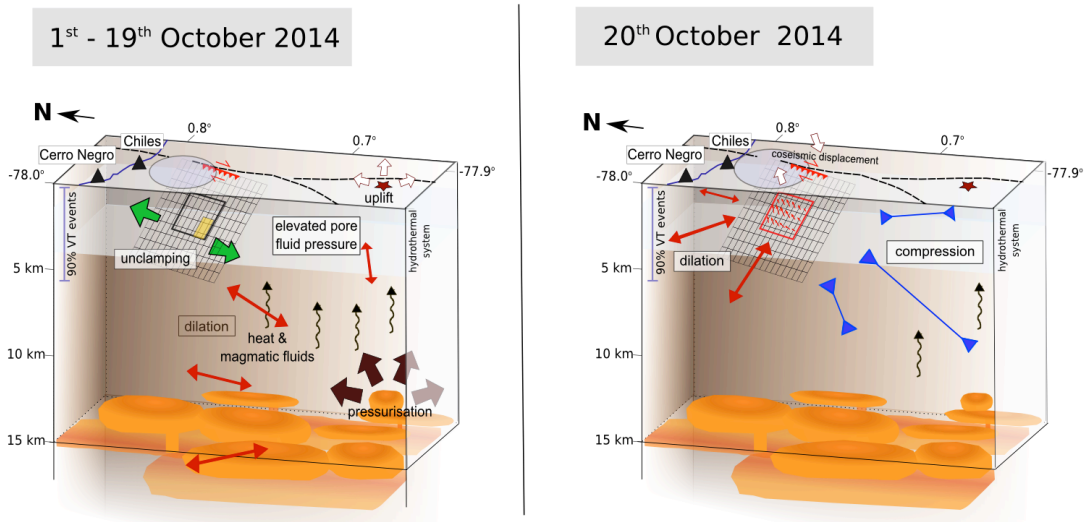

References

Albino, F., & Sigmundsson, F. (2014). Stress transfer between magma bodies: Influence of intrusions prior to 2010 eruptions at Eyjafjallajökull volcano, Iceland. Journal of Geophysical Research: Solid Earth, 119(4), 2964-2975. doi:10.1002/2013JB010510

Altamimi, Z., Collilieux, X., & Métivier, L. (2011). ITRF2008: an improved solution of the international terrestrial reference frame. Journal of Geodesy, 85(8), 457-473. doi:10.1007/s00190-011-0444-4

Battaglia, J., Métaxian, J. P., & Garaebiti, E. (2012). Earthquake-volcano interaction imaged by coda wave interferometry. Geophysical Research Letters, 39(11). doi:10.1029/2012GL052003

Beauval, C., Yepes, H., Bakun, W. H., Egred, J., Alvarado, A., & Singaucho, J. C. (2010). Locations and magnitudes of historical earthquakes in the Sierra of Ecuador (1587–1996). Geophysical Journal International, 181(3), 1613-1633. doi:10.1111/j.1365-246X.2010.04569.x

Benoit, J. P., & McNutt, S. R. (1996). Global volcanic earthquake swarm database and preliminary analysis of volcanic earthquake swarm duration. Annals of Geophysics, Vol 39(2). doi:10.4401/ag-3963. doi: 10.4401/ag-3963

510

511 Bettinelli, P., Avouac, J. P., Flouzat, M., Bollinger, L., Ramillien, G., Rajaure, S., & Sapkota, S.

512 (2008). Seasonal variations of seismicity and geodetic strain in the Himalaya induced by surface

513 hydrology. Earth and Planetary Science Letters, 266(3), 332-344. doi:10.1016/j.epsl.2007.11.021.

514

515 Biggs, J., Amelung, F., Gourmelen, N., Dixon, T. H., & Kim, S. W. (2009). InSAR observations of

516 2007 Tanzania rifting episode reveal mixed fault and dyke extension in an immature continental rift.

517 Geophysical Journal International, 179(1), 549-558. doi:10.1111/j.1365-246X.2009.04262.x

518

519 Biggs, J., Bastow, I. D., Keir, D., & Lewi, E. (2011). Pulses of deformation reveal frequently recurring

520 shallow magmatic activity beneath the Main Ethiopian Rift. Geochemistry, Geophysics, Geosystems,

521 12(9). doi: 10.1029/2011GC003662

522

523 Biggs, J., Chivers, M., & Hutchinson, M. C. (2013). Surface deformation and stress interactions during

524 the 2007–2010 sequence of earthquake, dyke intrusion and eruption in northern Tanzania. Geophysical

525 Journal International, 195(1), 16-26. doi:10.1093/gji/ggt226

526

527 Chen, C.W. and Zebker, H.A., 2002. Phase unwrapping for large SAR interferograms: statistical

528 segmentation and generalized network models. Geoscience and Remote Sensing, IEEE Transactions

529 on, 40(8), pp.1709-1719. doi:10.1109/TGRS.2002.802453

530

531 Chouet, B.A., and R.S. Matoza (2013), A multi-decadal view of seismic methods for detecting

532 precursors of magma movement and eruption, J. Volcanol. Geotherm. Res., 252, 108-175,

533 doi:10.1016/j.jvolgeores.2012.11.013

534

535 Cortés, G. P. and Calvache Velasco, M. L. (1997). Informe sobre la Evaluación de la Amenzana

536 Volcánica del Chiles y Cerro Negro. Répública de Colombia Ministerio de Mina Y Energía, Instituto

537 de investigaciones en Geociencias, Mineria y Química, Observatorio Vulcanológico y Sismologico de

538 Pasto.

539

540 Diez, M., La Femina, P. C., Connor, C. B., Strauch, W., & Tenorio, V. (2005). Evidence for static

541 stress changes triggering the 1999 eruption of Cerro Negro Volcano, Nicaragua and regional aftershock

542 sequences. Geophysical Research Letters, 32(4). doi: 10.1029/2004GL021788

543

544 Ego, F., Sébrier, M., Lavenu, A., Yepes, H., & Egues, A. (1996). Quaternary state of stress in the

545 Northern Andes and the restraining bend model for the Ecuadorian Andes. Tectonophysics, 259(1),

546 101-116. doi:10.1016/0040-1951(95)00075-5

547

548 Elliott, J. R., Walters, R. J., England, P. C., Jackson, J. A., Li, Z., & Parsons, B. (2010). Extension on
549 the Tibetan plateau: recent normal faulting measured by InSAR and body wave seismology.
550 Geophysical Journal International, 183(2), 503-535. doi:10.1111/j.1365-246X.2010.04754.x
551
552 Funning, G. J., B. Parsons, T. J. Wright, J. A. Jackson, and E. J. Fielding, (2005).Surface displacements
553 and source parameters of the 2003 Bam (Iran) earthquake from ENVISAT advanced synthetic aperture
554 radar imagery, Journal of Geophysical Research, 110(B9), B09,406, doi:10.1029/2004JB003338.
555
556 Jay, J. A., Delgado, F. J., Torres, J. L., Pritchard, M. E., Macedo, O., & Aguilar, V. (2015).
557 Deformation and seismicity near Sabancaya volcano, southern Peru, from 2002 to 2015. Geophysical
558 Research Letters, 42(8), 2780-2788. doi: 10.1002/2015GL063589
559
560 Hanssen, R. F. (2001). Radar interferometry: data interpretation and error analysis (Vol. 2). Springer
561 Science & Business Media.
562
563 Hill, D. P. (2006). Unrest in Long Valley Caldera, California, 1978–2004. Geological Society, London,
564 Special Publications, 269(1), 1-24. doi: 10.1144/GSL.SP.2006.269.01.02
565
566 Instituto Geofisico Escuela Nacional Politecnica, (2014) Informe del volcán Chiles – Cerro Negro N.-
567 23. www.igepn.edu.ec/chiles-cerro-negro/informes-chiles-cerro-negro/ccn-especiales.

Jónsson, S. (2009). Stress interaction between magma accumulation and trapdoor faulting on Sierra Negra volcano, Galápagos. Tectonophysics, 471(1), 36-44. doi:10.1016/j.tecto.2008.08.005

Jolly, A. D., & McNutt, S. R. (1999). Seismicity at the volcanoes of Katmai National Park, Alaska; July 1995–December 1997. Journal of volcanology and geothermal research, 93(3), 173-190. doi:10.1016/S0377-0273(99)00115-8

King, R. W., and Y. Bock. (1999). Documentation for the GAMIT GPS analysis software. Mass. Inst. of Technol., Cambridge Mass

Linde, A. T., & Sacks, I. S. (1998). Triggering of volcanic eruptions. Nature, 395(6705), 888-890. doi:10.1038/27650

Lin, J., & Stein, R. S. (2004). Stress triggering in thrust and subduction earthquakes and stress interaction between the southern San Andreas and nearby thrust and strike-slip faults. Journal of Geophysical Research: Solid Earth (1978–2012), 109(B2). doi: 10.1029/2003JB002607

Lu, Z., & Dzurisin, D. (2014). InSAR imaging of Aleutian volcanoes: monitoring a volcanic arc from space. Springer Science & Business Media. doi: 10.1007/978-3-642-00348-6_6

588

589 Maccaferri, F., Rivalta, E., Passarelli, L., & Aoki, Y. (2016). On the mechanisms governing dike arrest:

590 Insight from the 2000 Miyakejima dike injection. Earth and Planetary Science Letters, 434, 64-74.

591 doi:10.1016/j.epsl.2015.11.024

592

593 Manga, M., & Brodsky, E. (2006). Seismic triggering of eruptions in the far field: volcanoes and

594 geysers. Annual Reviews of Earth and Planetary Science, 34, 263-291. doi:

595 10.1146/annurev.earth.34.031405.125125

596

597 Moran, S., Stihler, S. and Power, J., (2002). A tectonic earthquake sequence preceding the April–May

598 1999 eruption of Shishaldin Volcano, Alaska. Bulletin of Volcanology, 64(8), pp.520-524. doi:

599 10.1007/s00445-002-0226-1

600

601 Moran, S. C., Newhall, C., & Roman, D. C. (2011). Failed magmatic eruptions: late-stage cessation of

602 magma ascent. Bulletin of Volcanology, 73(2), 115-122. doi: 10.1007/s00445-010-0444-x

603

604 Mothes, P. A., Nocquet, J. M., & Jarrín, P. (2013). Continuous GPS Network Operating Throughout

605 Ecuador. Eos, Transactions American Geophysical Union, 94(26), 229-231. doi:

606 10.1002/2013EO260002

607

608 Nishimura, T., Fujiwara, S., Murakami, M., Tobita, M., Nakagawa, H., Sagiya, T. and Tada, T., (2001).
609 The M6. 1 earthquake triggered by volcanic inflation of Iwate volcano, northern Japan, observed by
610 satellite radar interferometry. Geophysical Research Letters, 28(4), pp.635-638. doi:
611 10.1029/2000GL012022
612
613 Nocquet, J. M., Villegas-Lanza, J. C., Chlieh, M., Mothes, P. A., Rolandone, F., Jarrin, P., D. Cisneros,
614 A. Alvarado,L. Audin, F. Bondoux, X. Martin, Y. Font, M. Régnier, M. Vallée, T. Tran, C. Beauval, J.
615 M. Maguiña Mendoza, W. Martinez, H. Tavera & H. Yepes (2014). Motion of continental slivers and
616 creeping subduction in the Northern Andes. Nature Geoscience, *7*(4), 287-291. doi:
617 10.1038/NGEO2099
618
619 Okada, Y. (1985). Surface deformation due to shear and tensile faults in a half-space. Bulletin of the
620 seismological society of America, 75(4), 1135-1154.
621
622 Passarelli, L., Maccaferri, F., Rivalta, E., Dahm, T., & Boku, E. A. (2013). A probabilistic approach for
623 the classification of earthquakes as 'triggered'or 'not triggered'. Journal of Seismology, 17(1), 165-
624 187. doi:10.1007/s10950-012-9289-4
625

626 Pritchard, M. E., Jay, J. A., Aron, F., Henderson, S. T., & Lara, L. E. (2013). Subsidence at southern
627 Andes volcanoes induced by the 2010 Maule, Chile earthquake. Nature Geoscience, 6(8), 632-636,
628 doi:10.1038/ngeo1855.
629
630 Pritchard, M. E., and M. Simons. (2004) An InSAR‐based survey of volcanic deformation in the
631 central Andes. Geochemistry, Geophysics, Geosystems 5, no. 2. doi:10.1029/2003GC000610
632
633 Riel, B., Milillo, P., Simons, M., Lundgren, P., Kanamori, H., & Samsonov, S. (2015). The collapse of
634 Bárðarbunga caldera, Iceland. Geophysical Journal International, 202(1), 446-453.
635 doi:10.1093/gji/ggv157
636
637 Roman, D. C., & Power, J. A. (2011). Mechanism of the 1996–97 non-eruptive volcano-tectonic
638 earthquake swarm at Iliamna Volcano, Alaska. Bulletin of Volcanology, 73(2), 143-153. doi:
639 10.1007/s00445-010-0439-7
640
641 Rosen, P., Lavalle, M., Pi, X., Buckley, S., Szeliga, W., Zebker, H. and Gurrola, E., 2011, July.
642 Techniques and tools for estimating ionospheric effects in interferometric and polarimetric SAR data.
643 In Geoscience and Remote Sensing Symposium (IGARSS), 2011 IEEE International (pp. 1501-1504).
644 IEEE. doi: 10.1109/IGARSS.2011.6049352
645

Rosen, P., Eineder, M., Rabus, B., Gurrola, E., Hensley, S., Knoepfle, W., Breit, H., Roth, A. and Werner, M., 2001. SRTM-Mission-cross comparison of X and C band data properties. In Geoscience and Remote Sensing Symposium, 2001. IGARSS'01. IEEE 2001 International (Vol. 2, pp. 751-753). IEEE. doi: 10.1109/IGARSS.2001.976624

Rubinstein, J. L., La Rocca, M., Vidale, J. E., Creager, K. C., & Wech, A. G. (2008). Tidal modulation of nonvolcanic tremor. Science, 319(5860), 186-189. doi:10.1126/science.1150558

Ruiz, G., Cordova, A., Ruiz, M., and Alvarado, A. (2013). Informe Tecnico de los Volcanes Cerro Negro y Chiles. Technical report, IG-EPN.

Salvage, R. (2015). Using Seismic Signals to Forecast Volcanic Processes. PhD Thesis, Univeristy of Leeds.

Boletín Mensual No. 04-2014 - Periodo evaluado: Abril de 2014 (2014). Servicio Geológico Colombiano, Observatorio Vulcanológico y Sismológico de Pasto (OCSP). http://www2.sgc.gov.co/Pasto/Publicaciones/Reportes-de-actividad/Reportes-Mensuales---Boletines-Informativos/2014.aspx

665 Shuler, A., Nettles, M., & Ekström, G. (2013). Global observation of vertical-CLVD earthquakes at
666 active volcanoes. Journal of Geophysical Research: Solid Earth, 118(1), 138-164. doi:
667 10.1029/2012JB009721
668
669 Stein, R. S. (1999). The role of stress transfer in earthquake occurrence. *Nature*, *402*(6762), 605-609.
670 doi:10.1038/45144
671
672 Takada, Y., & Fukushima, Y. (2013). Volcanic subsidence triggered by the 2011 Tohoku earthquake in
673 Japan. Nature Geoscience, 6(8), 637-641. doi:10.1038/ngeo1857
674
675 Toda, S., Stein, R. S., & Sagiya, T. (2002). Evidence from the AD 2000 Izu islands earthquake swarm
676 that stressing rate governs seismicity. Nature, 419(6902), 58-61. doi:10.1038/nature00997
677
678 Vallée, M., J. Charléty, A.M.G. Ferreira, B. Delouis, and J. Vergoz, (2011) SCARDEC : a new
679 technique for the rapid determination of seismic moment magnitude, focal mechanism and source time
680 functions for large earthquakes using body wave deconvolution, Geophysical Journal International,
681 184, 338-358. doi: 10.1111/j.1365-246X.2010.04836.x
682

683 Vidale, J. E., Boyle, K. L., & Shearer, P. M. (2006). Crustal earthquake bursts in California and Japan:
684 Their patterns and relation to volcanoes. Geophysical Research Letters, 33(20).
685 doi:10.1029/2006GL027723
686
687 Wegmuller, U., Werner, C. and Strozzi, T., 1998, July. SAR interferometric and differential
688 interferometric processing chain. In International Geoscience And Remote Sensing Symposium (Vol.
689 2, pp. 1106-1108). Institute Of Electrical & Electronicsengineers, Inc (IEE).
690 doi:10.1109/IGARSS.1998.699687
691
692 White, R., & McCausland, W. (2016). Volcano-tectonic earthquakes: A new tool for estimating
693 intrusive volumes and forecasting eruptions. Journal of Volcanology and Geothermal Research, 309,
694 139-155. doi:10.1016/j.jvolgeores.2015.10.020
695
696 Wicks, C. W., Thatcher, W., Dzurisin, D., & Svarc, J. (2006). Uplift, thermal unrest and magma
697 intrusion at Yellowstone caldera. Nature, 440(7080), 72-75. doi:10.1038/nature04507
698
699 Wicks, C., de La Llera, J. C., Lara, L. E., & Lowenstern, J. (2011). The role of dyking and fault control
700 in the rapid onset of eruption at Chaitén volcano, Chile. Nature, 478(7369), 374-377.
701 doi:10.1038/nature10541
702

Wright, T. J., Ebinger, C., Biggs, J., Ayele, A., Yirgu, G., Keir, D., & Stork, A. (2006). Magma-maintained rift segmentation at continental rupture in the 2005 Afar dyking episode. Nature, 442(7100), 291-294. doi:10.1038/nature04978

Xu, W., S. Jónsson, F. Corbi and E. Rivalta, Graben formation and dike arrest during the 2009 Harrat Lunayyir dike intrusion: Insights from InSAR, stress calculations and analog experiments, J. Geophys. Res. (in revision), 2016. doi:10.1002/2015JB012505

Yang, X.M., Davis, P.M. and Dieterich, J.H., 1988. Deformation from inflation of a dipping finite prolate spheroid in an elastic half-space as a model for volcanic stressing. Journal of Geophysical Research: Solid Earth, 93(B5), pp.4249-4257. doi:10.1029/JB093iB05p04249

Yokoyama, I., 2001. The largest magnitudes of earthquakes associated with some historical volcanic eruptions and their volcanological significance. Annali di Geofisica, Vol 44, N 5/6. doi: 10.4401/ag-3553.

Acknowledgements

We thank all of the staff at the Instituto Geofisico in Quito Ecuador who have worked on monitoring the unrest at Chiles-Cerro Negro, including instrument deployment and maintenance,

data processing and field observations. The IGEPN expresses thanks to UNAVCO for support in GPS instrumentation and the SENPLADES Project provided funding for instrumentation and logistics. SKE and JB were supported by STREVA (NERC grant number: NE/J020052/1) and SKE, JRE and JB also by the Centre for the Observations and Modelling of Earthquakes, Volcanoes & Tectonics (COMET). SKE is now funded by a European Space Agency Living Planet Fellowship (IMRICA). JMN is supported by the IRD-France in the framework of the International Joint Laboratory Earthquakes & Volcanoes in the Northern Andes. The Committee for Earth Observation Satellite Volcano Pilot project provided CosmoSkymed (ASI) and TerraSAR-X (DLR) imagery. RADARSAT-2 data were provided by the Canadian Space Agency. We thank Mario Ruiz, Rebecca Salvage, Stephen Hernandez and Rowena Lohman for very helpful conversations. This work forms part of the CEOS Volcano Pilot for Disaster Risk Reduction.